

# Investigations of Sizes and Dynamical Motions of Solar Photospheric Granules by a Novel Granular Segmenting Algorithm

Yanxiao Liu<sup>1</sup>, Chaowei Jiang<sup>1</sup>, Ding Yuan<sup>1</sup>, Pingbing Zuo<sup>1</sup>, Yi Wang<sup>1</sup>, and Wenda Cao<sup>2,3</sup>

Institute of Space Science and Applied Technology, Harbin Institute of Technology, Shenzhen, Guangdong 518055, People's Republic of China; liuyanxiao303@163.com, chaowei@hit.edu.cn, yuanding@hit.edu.cn

New Jersey Institute of Technology, Center for Solar Research, 323 Martin Luther King Boulevard, Newark, NJ, USA

Big Bear Solar Observatory, 40386 North Shore Lane, Big Bear City, CA, USA

Received 2021 June 18; revised 2021 October 7; accepted 2021 October 7; published 2021 December 16

### **Abstract**

Granules observed in the solar photosphere are believed to be convective and turbulent, but the physical picture of the granular dynamical process remains unclear. Here we performed an investigation of granular dynamical motions of full length scales based on data obtained by the 1 m New Vacuum Solar Telescope and the 1.6 m Goode Solar Telescope. We developed a new granule segmenting method, which can detect both small faint and large bright granules. A large number of granules were detected, and two critical sizes, 265 and 1420 km, were found to separate the granules into three length ranges. The granules with sizes above 1420 km follow Gaussian distribution, and demonstrate *flat* in flatness function, which shows that they are non-intermittent and thus are dominated by convective motions. Small granules with sizes between 265 and 1420 km are fitted by a combination of power-law function and Gauss function, and exhibit nonlinearity in flatness function, which reveals that they are in the mixing motions of convection and turbulence. Mini granules with sizes below 265 km follow the power-law distribution and demonstrate linearity in flatness function, indicating that they are intermittent and strongly turbulent. These results suggest that a cascade process occurs: large granules break down due to convective instability, which transports energy into small ones; then turbulence is induced and grows, which competes with convection and further causes the small granules to continuously split. Eventually, the motions in even smaller scales enter in a turbulence-dominated regime.

Unified Astronomy Thesaurus concepts: Solar photosphere (1518); Solar granules (1875)

### 1. Introduction

Granules are overshoots of convective motions from the subphotosphere, and their patterns are formed by granule lanes where cold mass drops backward to the convection zone (Rast 1995; Stein & Nordlund 1998). They are considered highly dynamic and turbulent, characterized by random motions and large Reynolds numbers. With high values of Reynolds numbers, vortices are generated due to shear instability, and energy is transported from large-scale eddies and vortices to small-scale ones and down to microscale ones. At last, they are dissipated by viscosity. This cascade process could cause the population of granule cells to increase significantly with the decreasing scales, which is often described by the relationship between the energy and wavenumber of  $E_k \sim k^{-5/3}$ , according to the theory of a Kolmogorov spectrum (Kolmogorov 1941, 1991) under the assumption of isotropic and homogeneous turbulence in threedimensions.

According to Kolmogorov theory, the relationship of  $P \sim A^{D/2}$ , between perimeter (P) and area (A) of turbulent cells, is predicted with fractal dimension D of  $\frac{5}{3}$  for isotherms (Mandelbrot 1977) and of  $\frac{4}{3}$  for isobars (Lovejoy 1982). Roudier & Muller (1986) found the fractal dimension values of 1.25 and 2.15 with granule sizes smaller and larger than 1".37, respectively. Hirzberger et al. (1997) obtained a similar result with fractal dimension values of 1.3 and 2.1 for granule sizes smaller and larger than 1".39, respectively. Roudier & Muller (1986) explained that the granules with sizes smaller than 1".37 might be the turbulent origin, and the granules with sizes larger than 1".37 are convective. They further suggested that, if the

small granules are turbulent, it is necessary to classify the granules into convective and turbulent. Namely, the large and middle ones are granule cells, and the small ones are photospheric turbulent elements. Although Brandt et al. (1991) and Greimel et al. (1990) confirmed these results, they argued that there is no obvious evidence to support the small granules being the turbulent origin since the fractal dimension value might be strongly affected by technical problems, i.e., the limited resolution, the definition of granules, and so on. To avoid the uncertainties caused by granular segmenting thresholds, telescope limited resolution, as well as other possible factors, Abramenko et al. (2012) calculated the flatness function, which is a method of measuring the intermittency and multifractality (Abramenko 2005; Abramenko & Yurchyshyn 2010), and confirmed the results of Roudier & Muller (1986). Abramenko et al. (2012) found that the size distribution of large granules follows the Gauss function, and these large granules are non-intermittent. These regular granules represent dominant granules with sizes larger than 1000 km (Roudier & Muller 1986). The mini-granules follow power-law distribution with an index of  $-1.82 \pm 0.12$ , and they are considered to be highly intermittent and multifractal with sizes below 600 km.

Additionally, the power spectra of velocity fluctuations and intensity fluctuations, which represent the kinetic and thermal energies of granules, follow power-law functions with slopes of  $-\frac{5}{3}$  and  $-\frac{17}{3}$ , and thus reveal a turbulent cascade process of energy transportation from large granule cells to small ones (Salucci et al. 1994; Espagnet et al. 1995). Nevertheless, Petrovay (2001) pointed out that the physical conditions dominating in the photosphere are strongly inhomogeneous and

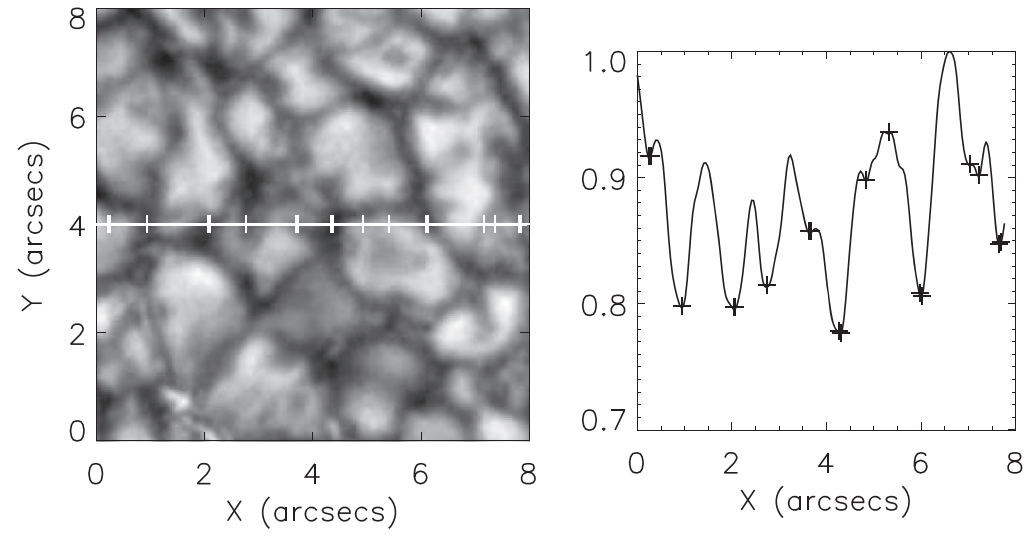


**Figure 1.** A small image contains granules and granule lanes. Left panel presents a small image that contains a few granules and granule lanes. A dashed line crosses granules and granule lanes, and the white plus signs on the dashed line marks the local intensity valley position in the *x* direction. Right panel gives the intensity variation along the dashed line, and the black plus signs correspond to the positions marked by white plus signs in the left panel.

anisotropic, and are more complicated than the turbulent state described by Kolmogorov theory.

As such, the dynamics of fluid motions, including convective and turbulent motions in the photosphere, are still under debate and more detailed studies are required. To help understanding the granular dynamical process, we first developed a new granule segmenting algorithm and then detected two critical size points separating the granular dynamical motions into three regimes: convection, mixing motions of convection and turbulence, and turbulence. This paper is organized as follows: Section 2 describes the observations and data processing, Section 3 describes the segmentation method, Section 4 presents the results and discussions, and Section 5 gives a conclusion of this work.

## 2. Observations and Data Processing

Two data sets are analyzed in this work, and the first one was obtained by New Vacuum Solar Telescope (NVST) at TiO (7058 Å) wavelength on 2019 November 27 in the Fuxian Solar Observatory (FSO; Liu et al. 2014). The very good and stable seeing in FSO allows the spatial resolution of NVST to achieve 0.72, which is close to the diffraction-limit resolution. The observation was chosen in a quiet region near the disk center with a field of view of 99.72 × 82.72, a cadence of 30 s, and a pixel size of 0.72039. The selected data were first processed with dark current subtraction and flat-field correction, and then reconstructed with the speckle masking method (Xiang et al. 2016). At last, a high-precision alignment was further applied to the reconstructed data (Feng et al. 2012; Yang et al. 2015; Wang & Xu 2020).

The second data set was taken by the 1.6 m Goode Solar Telescope (GST; Cao et al. 2010; Goode & Cao 2012) at a wavelength of TiO 7057 Å on 2019 October 3 at the Big Bear Solar Observatory (BBSO). The data were obtained in a very quiet region near the disk center, and they were taken under a very good seeing condition with the assistance of adaptive optics (Cao et al. 2010; Shumko et al. 2014), which allows the spatial resolution of GST close to 0."1. The field of view is  $69'' \times 69''$ , and the cadence is 10 s. Images own a very high quality and have a pixel size of 0."034 after reconstruction

(Wöger & von der Lühe 2007). We selected these two data sets and try to analyze the dynamics of granules by data of different spatial resolutions.

## 3. Method of Segmentation and Identifying Granules

In order to extract the granule cells, a method of segmentation and identifying granules is developed. The segmentation step aims to partition the image into individual and disjointed regions that contain target features (Hossain & Chen 2019), like granules or magnetic features, and the identifying step is to distinguish granules from magnetic features. Here, edge-based techniques (Kundu & Pal 1986; Shih & Cheng 2004), considering edges as boundaries and regions where properties change, are applied to segment granules. Usually, the edges of a feature could be distinguished by high-intensity gradients and large intensity discontinuities, as well as large intensity variations. Granule cells and magnetic features in the photospheric quiet regions are both located in dark granule lanes, and thus the edges could be easily detected. In this work, the segmentation is implemented by finding the edges of these features in the granule lanes according to their intensity variations. A few steps, including segmenting and distinguishing granules from magnetic features, are described in the following.

(1) Granular edge detection. Pixels that possess the lowest local intensity values in either x, y, or diagonal directions are extracted and labeled as the edges of granules and magnetic features. A sample showing the intensity variation along the x direction is given in Figure 1. The *edge pixels* of granules in the left panel marked with white plus signs correspond to local intensity valleys marked with black plus signs in the right panel, which indicates that the edge pixels could be detected by finding the local intensity valleys very easily. By taking this method, all edge pixels are extracted and the results are given with the edges marked in black in the middle panel of Figure 2.

We notice that most of these edge pixels are in granule lanes, and they connect to each other. A few of them, however, are isolated by these granule lanes and locate on the granules. We need to distinguish whether they are real edge pixels or part of granules, and then discard the false edge pixels. The edge

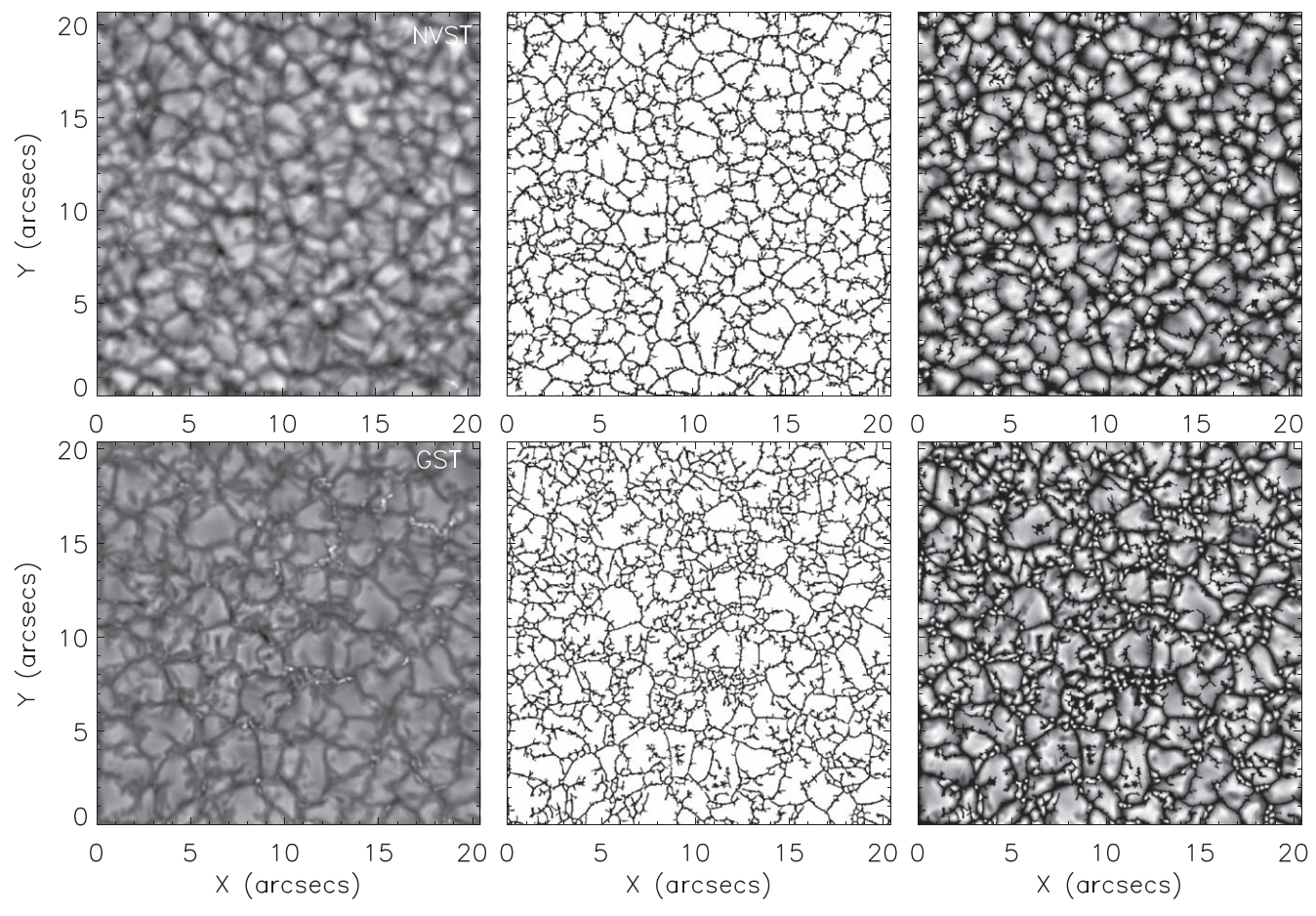


Figure 2. Segment results. The top and bottom rows are the original image, edge detection, and the segmenting result from the left to right panels for NVST and GST data, respectively.

pixels with an intensity higher than  $\mu+\sigma$  are actually bright pixels on granules, and hereby are false edge pixels. Here the  $\mu$ and  $\sigma$  are the mean and standard deviation of intensity of the image. The edge pixels with an intensity lower than  $\mu - \sigma$  are found to locate in the granule lanes and are considered to be real edge pixels. However, the edge pixels with an intensity in the range of  $\mu - \sigma$  to  $\mu + \sigma$  contain both real edge pixels and some false edge pixels. The false edge pixels in such an intensity range locate in the region where granules newly appear, and their intensity is originally reduced due to plasma cooling down. Such pixels should be discarded since it may cause over-segmentation. A proper size threshold is chosen to take these pixels away, e.g., the edges possessing pixels less than 200 for NVST data are discarded, while the remaining pixels are considered to be real edges of photospheric features. Most of the granules are surrounded by these edge pixels and are isolated into individual ones. However, a few of them still connect to each other by sharing a few common pixels. Further steps are needed to disconnect the connecting parts among individual features.

(2) Separation of closely connecting granules by morphology operations. When two granules stay very close and share common pixels with little intensity variations, part of the edges of these two granules overlap, namely the common edges, and they are difficult to detect. There are some well-established methods of edge detection, such as the Prewitt, Sobel, Marr–Hildreth, and Canny detectors (Gonzalez & Woods 2017), these methods mainly search edge pixels by finding the regions

where the first-order gradients reach their maximums or the second-order gradients change their signs. For example, the Canny detector is good at detecting the edges with obvious local gradients in the direction perpendicular to the edges, but is insensitive to the regions where the edge gradients are small. Meanwhile, the difficulty of edge detection in this work is searching for the edge pixels in the regions where their intensity fluctuation makes the edge gradients small. Thus, in such situations, the edges could not be found very well by detecting either the local intensity valley or large intensity gradients.

We notice that the common edges usually have a few pixels, which could be detected by reducing the boundary pixels of the granules a few times. Boundary pixels could be extracted by using erode and dilate operations (Gonzalez & Woods 2017). An erode operation discards the boundary pixels and fine structures by convolving a specific kernel with target features. Dilate takes an opposite operation that recoveries the boundary pixels of target features.

For every extracted blob, we need to first check whether it contains a single granule or multiple granules, and then make a judgment if we should further segment the granules contained in the blob. We first apply an erode operation, with a kernel of  $3 \times 3$ , twice to the blob. If the blob remains an isolated one after both the first and second erode operations, this blob is considered to contain an individual feature. If more than one of the smaller blobs appeared after the first or second erode operations, the extracted blob is considered to contain multiple

features by sharing some common edge pixels. For the blobs containing multiple granules, boundary pixels are marked by taking a few erode operations, and the overlapped pixels of two granules are searched by taking a few of the dilate operations. The detected common edges are discarded, and therefore the close connecting granules inside a blob are segmented successfully. The edge detection job is finished and the corresponding segmenting result is presented in the right panel of Figure 2.

(3) Distinguishing granule cells from magnetic features. Figure 2 shows us that the granules and magnetic features are successfully segmented. We are ready to distinguish granule cells and magnetic features. Magnetic features in the quiet Sun are mainly bright points and bright clusters in the granule lanes, which are characterized by a strong intensity gradient and small sizes. According to the segmenting results in the right panel of Figure 2, some bright points and bright clusters are separated from the granule lanes successfully. Even so, some of them are segmented to be part of the granules. In order to extract the pure granule cells, bright points are first identified with the method described in Liu et al. (2018), and then the blobs containing bright points are removed from the segment results.

## 4. Results and Discussions

The selected NVST data including a sequence of 48 images and GST data, which includes a sequence of 77 images, have been analyzed. A large number of granules have been successfully extracted with the novel segmenting method. The segmenting method has the ability of detecting both small faint and large bright granules owing to the edge detection method, which is developed to find the local lowest intensity values in specific directions and is independent of the intensity threshold. This makes the faint granules accessible, and based on which, the granules are in the full range of length scales. The dynamics of granules are analyzed with the distributions of length scale, perimeter, and *flatness* in Figures 3 and 4.

The length of a granule is measured by calculating its equivalent diameter while considering the granule as a round shape. Panels (a) and (b) of Figure 3 present the length-scale distribution of granules obtained by NVST data and GST data, which are fitted with different functions. For the plot in panel (a), the size in the range of 130-265 km is fitted by a powerlaw function with slope of -0.9; the size in the range of 265–1420 km is fitted by the sum of a power-law and a Gauss function in red solid line; and the size in the range of 1420-3000 km is fitted by a Gauss function. The subplot draws the power-law and Gauss functions in blue color, as well as their sum in black color. For the plot in panel (b), the size in the range of 170-265 km is fitted by a power-law function with slope of -1.8; the size in the range of 265–1420 km is fitted by the sum of a power-law and a Gauss function in red solid line; and the size in the range of 1420-3000 km is fitted by a Gauss function. The subplot shows their fitting functions as well. The power-law and Gauss fitting functions are expressed in Equations (1) and (2):

$$Y_1 = C_1 x^k \tag{1}$$

$$Y_2 = C_2 \frac{1}{\sqrt{2\pi} \sigma} e^{\left(-\frac{1}{2}(\frac{x-\mu}{\sigma})^2\right)}.$$
 (2)

The goodness of fitting is also measured by calculating the Chi-Square ( $\chi^2$ ) with the formula (3):

$$\chi^2 = \sum \frac{(Y_i - Y_{\text{fit}_i})^2}{Y_i},$$
 (3)

where  $Y_i$  and  $Y_{\text{fit}_i}$  are the statistical and theoretical values. The fitting parameters and the measured Chi-Square ( $\chi^2$ ) are listed in Table 1.

The two critical size points at d1 = 265 km and d2 = 1420 km have been found and marked in both panels (a) and (b) with vertical dashed lines. They are obtained at the places where fitting functions change. According to panels (a) and (b) of Figure 3, these two critical size points might separate the motions of granules into three types: the convection, the mixing motions of convection and turbulence, and the turbulence. Furthermore, panel (b) of Figure 3 demonstrates almost linearly, and the power-law function plays a more and more important role, along with the length scale reducing in the mixing motion stage. This reveals that the motions of the granules become obviously turbulent with the decrease of length.

We notice that the distribution shapes in panels (a) and (b) are obviously different. The length-scale range from 265 to 1420 km in panel (b) behaves more linearly than that in panel (a). In such a length-scale range, the granules in panel (b) of Figure 3 are more turbulent than those in panel (a). Such an obvious discrepancy is probably caused by different spatial resolutions since the GST data possess a higher spatial resolution and it could provide more detailed information about the intensity variations of the granules. On the other hand, there are some granules with sizes smaller than 130 km in panel (a) and smaller than 170 km in panel (b), which drops off the linear fitting lines, and which occupies a quite high probability. This phenomenon is also reported by Roudier & Muller (1986), Hirzberger et al. (1997), Abramenko et al. (2012), and is considered being independent of granule segmenting methods. It is probably caused by the limited spatial resolutions, which might underestimate the population of tiny granules. The details of such tiny granules are beyond the scope of this work and will be analyzed in the future, hopefully with an even higher spatial resolution telescope, such as the Inouye Solar Telescope.

In addition, it is necessary to note here that the size threshold applied in the granule segmenting steps is different from the derived critical sizes. The size threshold in the granule segmenting algorithm is used to distinguish if the edge pixels are false edges or not. Usually the false pixels are part of granules, which are isolated by pixels in granule lanes when putting all these detected edge pixels into an empty array and setting them to a value of 1. A proper threshold could help discard the false edge pixels from all the detected edge pixels. One obvious difference between the critical sizes and the threshold size is that the former is a value of the granule size, and the latter is part of the granules that might develop into the edges of the granules.

We also calculated the flatness function, F(r), in this work to confirm the critical points obtained in the length-scale distribution plots. According to Abramenko et al. (2012), a sixth-order flatness function describes the ratio between the sixth-order structure function to the cube of the second-order structure function (Abramenko 2005; Abramenko & Yurchyshyn 2010; Abramenko et al. 2012), where the qth order

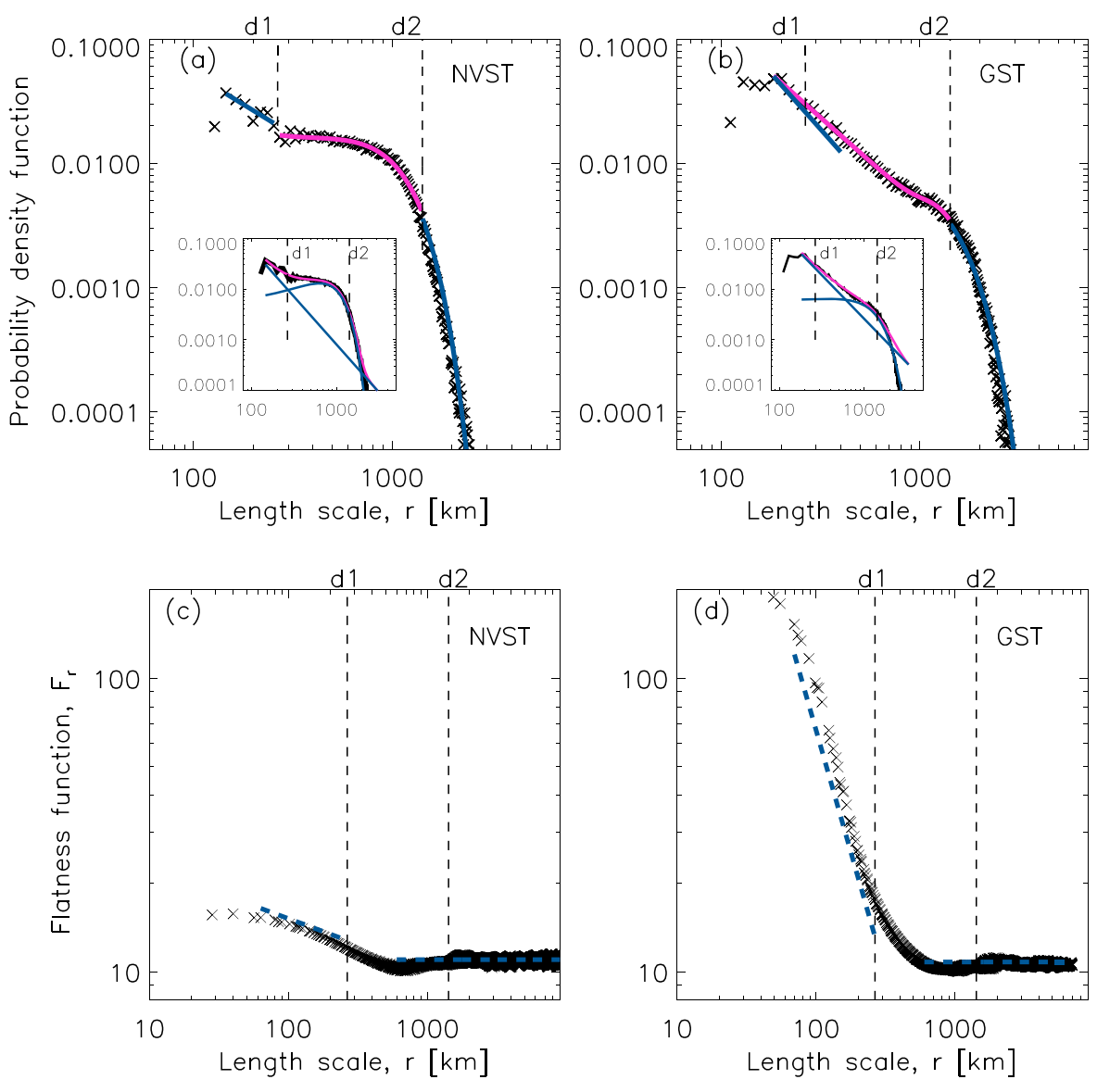


**Figure 3.** Histogram and flatness functions of granules. Panels (a) and (b) plot the length-scale distributions of granules with the NVST data and GST data, respectively. Two critical size points are marked in vertical dashed lines at d1 = 265 km and d2 = 1420 km. The blue and red real lines are fitting lines. The data are fitted by power-law functions, in the range of 130–265 km for NVST and 170–265 km for GST, and they are fitted by the sum of the power-law and Gauss functions in the range of 265–1420 km, and are fitted by Gauss function in the range of 1420–3000 km, respectively. The subplots in panels (a) and (b) are the distributions in black color, the fitting results for the data as a whole in red color, and the components of fitting functions in blue color, respectively. The critical points are marked at the points where fitting functions deviate from the distributions. Panels (c) and (d) are the logarithm plots of flatness function with the NVST data and GST data. The horizontal, blue dashed lines label the *flat* length scales of the granules, and the sloping dashed lines in blue mark the linearity length scales of the granules.

structure function  $S_q(r)$  could be written as qth power of the intensity increment between two pixels at (x+r) and x in distance r:

$$S_q(r) = |I(x+r) - I(x)|^q.$$
 (4)

The sixth-order flatness function, F(r), hereby, could be expressed as:

$$F(r) = \frac{\langle |I(x+r) - I(x)|^6 \rangle}{(\langle |I(x+r) - I(x)|^2 \rangle)^3},\tag{5}$$

where  $\langle \rangle$  stands for the mean value of the structure function in the whole image. The flatness could be used to measure the intermittency and multifractality of features. Intermittency and multifractality are the typical characteristics of turbulence. The linearity of flatness with a negative slope in a logarithm plot

reveals the multifractality and intermittency of features; while the *flat* shape of flatness, which is corresponding to Gaussian distribution, indicates no intermittency and no multifractality of features (Abramenko 2005; Abramenko & Yurchyshyn 2010).

The panels (c) and (d) of Figure 3 present the flatness functions obtained with NVST and GST data, respectively, which demonstrate linearity, nonlinearity, and flatness in three length-scale ranges separated by two critical points at 265 and 1420 km. The flatness functions with sizes larger than the critical point of 1420 km are flat, which indicate the granules of being non-intermittent, non-multifractal, and regular, and they correspond to the Gaussian distribution presented in panels (a) and (b) of Figure 3; the flatness functions demonstrate nonlinearity with sizes in the range of 265–1420 km, which correspond to the mixing motions of convection and turbulence

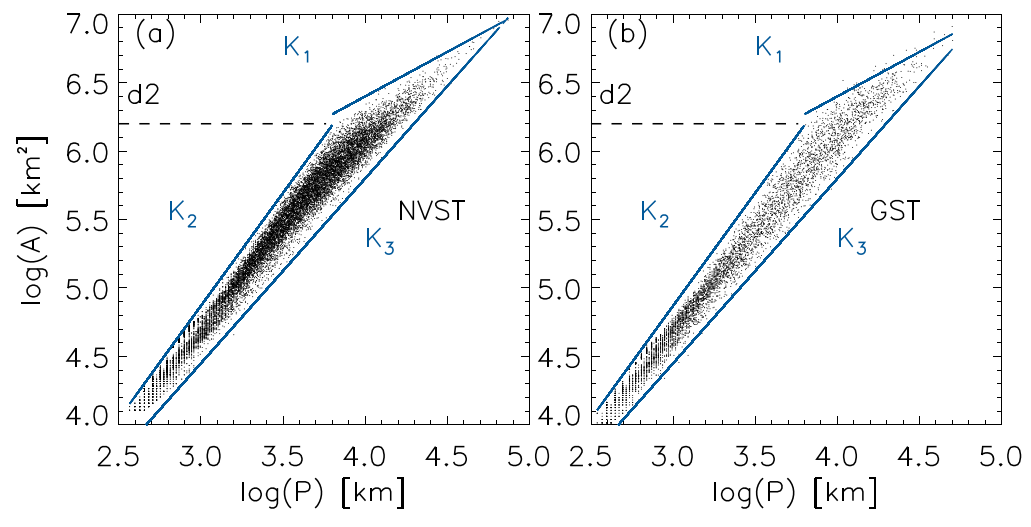


Figure 4. The P-A logarithm scatter plot. The left and right panels are plotted with the NVST data and GST data, respectively. The slopes are marked with  $K_1$ ,  $K_2$ , and  $K_3$  of 0.65, 1.65, and 1.35, respectively, and the critical size point at 1420 km is labeled at the place where the P-A logarithm plot linearly changes.

Table 1								
Fitting Parameters	of Diameter	and Area	Distribution					

	Length Ranges (km)	k	$C_1$	$C_2$	Mean $\mu$	Standard Deviation $\sigma$	Chi-Square $(\chi^2)$	Fitting Functions
	130–265	-0.98	4.8		•••		0.002	$Y_1$
NVST	265-1420	-1.4	14	19	517	548	0.002	$Y_1 + Y_2$
	1420-3000	•••	•••	19	517	548	0.004	$Y_2$
	170–265	-1.8	363				0.001	<i>Y</i> <sub>1</sub>
GST	265-1420	-1.8	363	15	629	467	0.001	$Y_1 + Y_2$
	1420-3000			15	629	467	0.001	$Y_1$

as revealed by the sum of the Gauss and power-law fitting functions in the same length range in panels (a) and (b) of Figure 3; and the flatness functions show linearity with negative slopes with sizes smaller than 265 km, which reveals the granule motions of being fully turbulent as described by power-law distributions in the panels (a) and (b) of Figure 3.

The flatness function presented in panel (d) shows more details than that in panel (c) due to the higher spatial resolution of GST. In the nonlinearity length-scale range, panel (d) shows the F(r) value vastly increases along with the granule size reducing. Correspondingly, the distribution in panel (b) of Figure 3 in the same length range appears nearly linear. This reveals that the process of transferring dynamics from convection to turbulence is dominant and significant.

Abramenko et al. (2012) also analyzed the GST data and reported two populations of granules: the regular granules with sizes larger than 1000 km are convective; the mini-granules with sizes smaller than 600 km are intermittent and turbulent. In general, this is in agreement with the results presented in panel (b) of Figure 3 in this work since the length-scale distribution of the granules in the mixing motion stage behaves strongly turbulent. The difference is that we classify this length range scale into a mixing motion stage, which combines the convection and turbulence motions. On the other hand, the critical point of 1420 km separates larger granules as regular are obtained at the point where the fitting function changes in this work, while the critical point of 1000 km is derived by the mean value of the Gauss fitting function in Abramenko et al. (2012). We also notice that previous studies separated the motions of granules into convection and turbulence by a single critical point (Roudier & Muller 1986; Greimel et al. 1990; Abramenko et al. 2012). The reliable granule segmenting method applied in this work and the high-quality data obtained by large aperture solar telescopes enable us to detect more details of granules, and hereby find the three regimes of motions, namely, convection, mixing motion of convection and turbulence, and turbulence. In these three regimes, the length-scale distribution of the granules follows the Gauss function, the sum of Gauss and power-law functions, and the power law, separately; and the corresponding flatness function demonstrates flatness, nonlinearity, and linearity, respectively.

Additionally, the fractal dimension, *D*, which could be used to measure the shape irregularity, is also calculated in this work by taking the following area-perimeter relation:

$$P = K \cdot A^{D/2} \tag{6}$$

where P, K, and A are perimeter, factor, and area, respectively. The P-A log-log scatter plots are presented in panels (a) and (b) of Figure 4 with the NVST data and GST data, respectively, which demonstrate a linear relationship with a sharp change at 1420 km. The slopes are found to vary in the ranges of [1.35, 1.65] and [0.65, 1.35] and the corresponding fractal dimensions D of [1.21, 1.48] and [1.48, 3.07] with sizes smaller and larger than 1420 km, respectively. This might indicate that the size at 1420 km is the separator between the regular granules and turbulent granules. Roudier & Muller (1986) found the fractal dimension D of 1.25 for granules smaller than 900 km (1.737). According to the Kolmogorov theory of predicting D of 5/3 and 4/3 for isotherms and isobars, respectively, they found that

D=1.25 is close to 4/3 and hereby suggested that the small scale granules (smaller than 1.1.37) are of a turbulent origin. Greimel et al. (1990) found D of 1.13 and 1.9 for granules smaller and larger than the critical size of 1.1.32, respectively, and they argued that the fractal dimension might not be correct for the small granules since the shapes of the small granules are roughly considered as round because of limited spatial resolution.

## 5. Conclusion

In this work, we studied the dynamical motions of photospheric granules with the high spatial resolution data from NVST and GST. To this end, we developed a new granule segmenting method, which enables us to identify the small faint granules located in the granule lanes as well as the large bright granules, thus allowing us to access the full length range of granules.

The length-scale distributions of the granules obtained with the NVST data and GST data have been studied, and two critical points at sizes of d1 = 265 km and d2 = 1420 km have been found. The critical point at the size of 265 km is determined at the cross point of the Gauss function and powerlaw function for the NVST data and at the point where the linear fitting deviates from the data for the GST data; the critical point at the size of 1420 km is determined at the point where the Gauss function starts to fit the length-scale distribution while the sum of the Gauss function and powerlaw function starts to deviate. The granules with the size larger than 1420 km can be fitted by the Gauss function and are thought to be dominated by convective motions. The granules with sizes in the range of 265–1420 km can be fitted by the sum of the Gauss function and power-law function, which indicates a mixing motion of the convection and turbulence. Though, in the mixing motion stage, the granules behave strongly turbulent as revealed by the GST data. Granules with a size smaller than 265 km can be fitted by the power-law function, suggesting that the *mini*-granules are fully turbulent. Correspondingly, the flatness functions plotted by both the NVST and GST data are flat, linear with negative slope, and nonlinear with granule sizes above 1420 km, below 265 km, and between 265 and 1420 km, respectively. In addition, the fractal dimension D has been analyzed through the A-P logarithm plot, and the critical point at 1420 km that separates the granule into the turbulence and stable convection.

In a summary, our analysis suggests that a cascade process occurs in the dynamical motions of granules: the large granules or regular granules are originally convective. They split and transport energy into small granules. Turbulent motions generate, start to grow, and compete with convective motions. The small granules continue to split into smaller ones. The turbulence becomes strong enough, overcomes the convective motion, and dominates the motions at last.

This work is supported by the National Natural Science Foundation of China (Nos. 41822404, 11973083, 42074205,

11803005, 12111530078, 12173012, and 4217040250) and Shenzhen Technology Project (JCYJ20190806142609035, GXWD20201230155427003-20200804151658001). We are grateful for the topic observation chance provided by the Fuxian Solar Observatory (FSO) and for the assistance with observations and data reconstructions provided by Professor Xu Zhi, observation assistants Luo Lin and Liao Guangquan, and the NVST team. We also thank the GST team for providing high-quality data. The BBSO operation is supported by NJIT and the USA NSF AGS-1821294 grant. The GST operation is partly supported by the Korea Astronomy and Space Science Institute, the Seoul National University, the Key Laboratory of Solar Activities of Chinese Academy of Sciences (CAS), and the Operation, Maintenance and Upgrading Fund of CAS for Astronomical Telescopes and Facility Instruments.

### **ORCID iDs**

Yanxiao Liu https://orcid.org/0000-0002-3921-1679 Chaowei Jiang https://orcid.org/0000-0002-7018-6862 Ding Yuan https://orcid.org/0000-0002-9514-6402 Pingbing Zuo https://orcid.org/0000-0003-4711-0306

#### References

```
Abramenko, V., & Yurchyshyn, V. 2010, ApJ, 722, 122
Abramenko, V. I. 2005, SoPh, 228, 29
Abramenko, V. I., Yurchyshyn, V. B., Goode, P. R., Kitiashvili, I. N., &
  Kosovichev, A. G. 2012, ApJL, 756, L27
Brandt, P. N., Greimel, R., Guenther, E., & Mattig, W. 1991, in Applying
  Fractals in Astronomy, ed. A. Heck & J. M. Perdang (Berlin: Springer), 77
Cao, W., Gorceix, N., Coulter, R., et al. 2010, AN, 331, 636
Espagnet, O., Muller, R., Roudier, T., Mein, N., & Mein, P. 1995, A&AS,
  109, 79
Feng, S., Deng, L., Shu, G., et al. 2012, in 2012 IEEE Fifth Int. Conf. on
  Advanced Computational Intelligence (ICACI) (Piscataway, NJ: IEEE), 626
Gonzalez, R. C., & Woods, G. E. 2017, Digital Image Processing (4th ed.;
  London: Pearson), 185
Goode, P. R., & Cao, W. 2012, Proc. SPIE, 8444, 844403
Greimel, R., Brandt, P. N., Guenther, E., & Mattig, W. 1990, VA, 33, 413
Hirzberger, J., Vázquez, M., Bonet, J. A., Hanslmeier, A., & Sobotka, M. 1997,
   ApJ, 480, 406
Hossain, M. D., & Chen, D. 2019, JPRS, 150, 115
Kolmogorov, A. 1941, DoSSR, 30, 301
Kolmogorov, A. N. 1991, RSPSA, 434, 9
Kundu, M., & Pal, S. 1986, PaReL, 4, 433
Liu, Y., Xiang, Y., Erdélyi, R., et al. 2018, ApJ, 856, 17
Liu, Z., Xu, J., Gu, B.-Z., et al. 2014, RAA, 14, 705
Lovejoy, S. 1982, Sci, 216, 185
Mandelbrot, B. B. 1977, The Fractal Geometry of Nature (San Francisco, CA:
   W. H. Freeman)
Petrovay, K. 2001, SSRv, 95, 9
Rast, M. P. 1995, ApJ, 443, 863
Roudier, T., & Muller, R. 1986, SoPh, 107, 11
Salucci, G., Bertello, L., Cavallini, F., Ceppatelli, G., & Righini, A. 1994,
  A&A, 285, 322
Shih, F. Y., & Cheng, S. 2004, Inf. Sci., 167, 9
Shumko, S., Gorceix, N., Choi, S., et al. 2014, Proc. SPIE, 9148, 914835
Stein, R. F., & Nordlund, A. 1998, ApJ, 499, 914
Wang, R., & Xu, Z. 2020, RAA, 20, 103
Wöger, F., & von der Lühe, O. 2007, ApOpt, 46, 8015
Xiang, Y.-y., Liu, Z., & Jin, Z.-y 2016, NewA, 49, 8
```

Yang, Y.-F., Qu, H.-X., Ji, K.-F., et al. 2015, RAA, 15, 569